Article:
Erman, S.C., Aydin, A., Groom, K. et al. (1 more author) (2025) Diode area melting of SS316L using low power 450 nm lasers. The International Journal of Advanced Manufacturing Technology, 136. pp. 4471-4490. ISSN 0268-3768

https://doi.org/10.1007/s00170-025-15090-0

The International Journal of Advanced Manufacturing Technology
https://doi.org/10.1007/s00170-025-15090-0

ORIGINAL ARTICLE

Diode area melting of SS316L using low power 450 nm lasers

Sefer Can Erman[1] · Alkim Aydin[1,3] · Kristian Groom[2] · Kamran Mumtaz[1]

Received: 28 October 2024 / Accepted: 19 January 2025

Abstract
This study investigates the use of Diode Area Melting (DAM) to process 316L stainless steel (SS316L), an alternative to Laser Powder Bed Fusion (LPBF), utilising independently addressable, low-power (~3.5 W) 450 nm blue lasers to address key limitations of LPBF, including thermal control, scalability, and efficiency. A normalised energy density (NED) processing map was developed to ensure successful material melting. Results demonstrated that DAM can achieve a relative density of 99.99% in single-layer SS316L samples using multiple 450 nm blue diode lasers. Notably, DAM-processed SS316L exhibited a significantly higher delta-ferrite content than samples produced via traditional LPBF, which is attributed to the slower cooling rate in DAM (600 °C/s vs. 10^7 °C/s). This increased delta-ferrite content enhances resistance to stress corrosion cracking in austenitic steel welds. Moreover, sub-grain cellular structures in the DAM-processed SS316L showed a 100% increase in size (4 µm) compared to those produced by LPBF.

Keywords Diode Area Melting (DAM) · Laser Powder Bed Fusion (LPBF) · Stainless Steel 316L (SS316L) · 450 nm diode lasers

1 Introduction

Laser Powder Bed Fusion (LPBF) is a widely used Additive Manufacturing (AM) technology for the fabrication of complex metallic components. LPBF fabricates three-dimensional parts by selectively melting feedstock material layer-by-layer using a rapidly scanning high-power fiber laser. LPBF is used to create components for several sectors such as the automobile and aerospace industries due to the ability to create lightweight components at a reduced lead time with a high design complexity [1]. However, LPBF technology has some challenges, such as rapid cooling and heating cycles created by the use of a fast-moving laser, which can cause residual stresses and distortion in parts [2]. Zavala-Arredondo et al. [3] also emphasised the scalability limitations of this methodology and the inefficient use of high-power and high-wavelength lasers within LPBF systems.

Diode Area Melting (DAM) is an alternative to traditional LPBF using multiple low-power (~3.5 W) short-wavelength fiber-coupled diode lasers to melt feedstock material. This method was developed at the University of Sheffield and has enabled the processing of Ti6Al4V powder with 808 nm and 450 nm diode lasers previously [4–6]. This paper presents, for the first time, an in-depth study of the capabilities of the technology when processing stainless steel 316L (SS316L), a material extensively researched and processed for industrial applications using LPBF. 316L's notable use in industry is due to its superior corrosion resistance [7], biocompatibility [8], strength, and cost-effectiveness [9]. SS316L is commonly preferred as an implant material in the medical field due to its excellent corrosion resistance and biocompatibility [10]. Further research is being conducted on surface treatments for SS316L implants, such as electropolishing [11] and ion implantation [10], to enhance their pitting resistance. Moreover, additively manufactured SS316L enables the production of complex geometries, making it suitable for scaffolds used in bone defect repair and joint replacements [12]. Additionally, the superior pitting resistance of SS316L makes it a preferred material for use in corrosive

✉ Sefer Can Erman
scerman1@sheffield.ac.uk

[1] School of Mechanical, Aerospace, and Civil Engineering, The University of Sheffield, Sheffield S1 4TD, UK

[2] School of Electrical and Electronic Engineering, The University of Sheffield, Sheffield S1 4TD, UK

[3] Faculty of Engineering, Department of Automotive Engineering, Cukurova University, Adana 01250, Turkey

Published online: 30 January 2025

environments, particularly in welding applications [13, 14]. Additionally, numerical studies have been conducted to optimize and model the welding process of austenitic stainless steel [15]. D'Andrea [16] reported that 40.7% of SS316L applications are in the petrochemical and chemical industries, 21.5% in marine onshore and offshore environments, 14.1% in biomedical applications, and 9.5% in the automobile sector.

The laser absorptivity of metal surfaces is found to be significantly influenced by the wavelength of the laser employed [17]. The absorptivity of Ti6Al4V powder was increased by 14% when employing an 808 nm diode laser during DAM compared to traditional LPBF [5]. Furthermore, an additional 11% increase was observed when 450 nm blue diode lasers were used in place of 808 nm diode lasers [5]. Brandau et al. [18] investigated the absorbance of 39 different powders, varying grain sizes, at 20 different laser wavelengths. The absorptivity of the SS316L powder was measured at 78.4% using 450 nm diode lasers and at 71.2% using 1070 nm fibre lasers [18].

The laser power requirement for the fabrication of multi-layer parts with LPBF is hundreds of watts [19–21], DAM enables the processing of single tracks and multi-layer parts with 3.5–4.5 W of power from a single-diode laser [5, 6] but scans across the powder bed at much lower speeds. In addition to laser power, it is important to discuss the differences in other process parameters, such as laser spot size, between DAM and traditional LPBF. Generally, the laser spot size in LPBF processing ranges from 50 µm to 200 µm [22–26]. In some cases, the laser spot size can increase up to 400 µm [27]. In DAM, the laser spot size cannot be determined in the same way as in LPBF due to the integration of multiple diode lasers. It is influenced by the number of lasers used in the processing and is certainly wider compared to traditional LPBF, particularly in the direction perpendicular to the scanning direction.

The cooling rate of LPBF is typically within the range of 10^3 to 10^8 K s^{-1} [28]. The cyclic thermal history (i.e. rapid cooling and heating) and cooling rate of the traditional LPBF process have a significant impact on the microstructure of the resulting parts [29]. Vysotskiy et al. validated the efficacy of reducing the cooling rate through building direction to observe α-martensite in 17–4 PH samples [30]. The rapid cooling rate of Ti6Al4V results in the formation of a ά martensite microstructure [31]. In contrast to traditional LPBF processes, the cooling rate in DAM is significantly lower, measured at 600 °C/s during the processing of Ti6Al4V [4]. The custom laser head assembly in DAM is intentionally designed to facilitate both preheating and post-heating, as well as remelting [4]. The remelting of the previously created track, facilitated by the laser beam geometry and hatch distance in DAM, leads to a slower cooling rate. This controlled cooling rate plays a crucial role in customising the microstructure of the parts. Caglar et al.[6] and Alsaddah et al.[5] successfully observed the β-phase in Ti6Al4V due to a slower cooling rate in DAM. Additionally, the elevated cooling rate associated with LPBF applications has the potential to preclude the observation of the second phase, namely δ-ferrite, in SS316L samples [32]. Nevertheless, rapid solidification has resulted in the formation of finer microstructures in the resulting parts [33]. The mechanical properties of LPBF parts with a finer microstructure than wrought samples, having higher yield strength and ultimate tensile strength [34].

The majority of LPBF studies employ the volumetric energy density (VED) formulation to analyse the effects of process parameters on the densification [35] and mechanical properties [36] of the produced parts. The VED formula, presented as Eq. 1, incorporates key process parameters such as P is laser power (W), v is scanning speed (mm/s), h is hatch distance (mm), and t is layer thickness (mm) [25].

$$E_v = \frac{P}{vht} \tag{1}$$

The VED formulation, which employs a limited number of factors (see Eq. 1), represents an appropriate methodology for comparing and evaluating energy density requirements in traditional LPBF applications involving fiber lasers. It is needed to adapt DAM to different energy density formulations which is independent of the type of processing. Thomas et al. [37] developed a normalised energy density (NED-E_0^*) equation which takes into account several material properties compared to VED. The multiplication of the dimensionless heat input per melt track (E^*) (see Eq. 2) and dimensionless hatch distance (h^*) (see Eq. 3) gives the last iteration of (NED-E_0^*) the formula that can be shown as Eq. 4.

$$E^* = \frac{q^*}{v^* l^*} \tag{2}$$

where q^* is a dimensionless beam power, v^* is a dimensionless scanning speed and l^* is a dimensionless layer thickness.

$$h^* = \frac{h}{r_b} \tag{3}$$

where h is the hatch distance (m) and r_b is the beam radius (m).

$$E_0^* = \frac{q^*}{v^* l^* h^*} = \frac{Aq}{2vlh} \frac{1}{\rho C_p (T_m - T_0)} \tag{4}$$

where A is the laser absorptivity of powder, ρ is the density (kg/m^3) of the powder, q is a laser power (W), l is a layer thickness (m), C_p is the specific heat (J/kg.K) of the powder,

T_m is the melting temperature (K) of the powder and T_0 is the initial temperature (K) of the system.

Table 1 illustrates the process parameters and NED – E_0^* values that have been calculated with Eq. 4 for LPBF studies processing SS316L. The process parameters mentioned have been demonstrated to successfully fabricate LPBF parts with a relative density exceeding ~ 99% (except references 1 and 2 in Table 1). As can be seen in Table 1, the process parameters including scanning speed, hatch distance, and spot size are selected from a range of options rather than adhering to a specific series of parameters. For instance, the scanning speed varies from 200 to 2000 mm/s, while the hatch distance ranges from 35 to 122 µm. The NED values exhibit a range of 3 to 15 for LPBF studies with SS316L. Furthermore, the Ti6Al4V powder, which was the sole material processed on DAM before this study, is illustrated in red circles in Fig. 1, following the literature on LPBF. The energy requirement of SS316L is greater than that of Ti6Al4V, due to the higher density of the former. In addition, the heat capacity of SS316L is approximately 5% lower than that of Ti6Al4V [6].

Figure 1 illustrates a normalised energy diagram for LPBF literature works processing SS316L. The ratio of dimensionless volumetric heat input per scan line (E^*) and hatch spacing (h^*) provides the normalised equivalent energy (E_0^*) (see Eq. 4). The literature works are represented by constant E_0^* contours, which are depicted by dashed lines in Fig. 1.

A slight modification was made by Alsaddah et al. [4] to adapt the shape of the laser array spot in the DAM system to the NED formula and Eq. 5 is used to obtain normalised hatch distance values in Eq. 3.

$$2r_b = (n * 2r) + (n - 1) * d_g \quad (5)$$

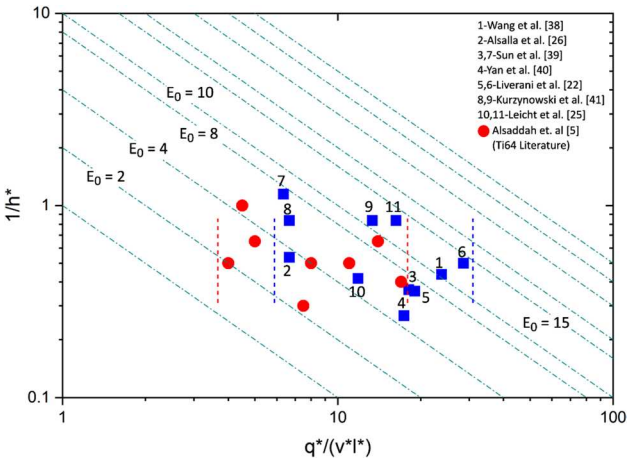

Fig. 1 Normalised energy density (NED), E_0^*, diagram according to data obtained from the literature (see Table 1) for SS316L (demonstrated with blue squares), and for Ti6Al4V (demonstrated with red circles)

where n is the number of lasers in the laser array, r is the radius of multiple laser spots (m), and d_g is the distance (m) between subsequent active laser spots in the laser array.

2 Materials and methods

2.1 Material specifications

In this study, SS316L powder which is supplied by Carpenter Additive is selected as a feedstock material. Table 2 shows the chemical composition of the powder which is obtained by the supplier. SS316L is distinguished from other 300

Table 1 Process parameters, relative densities, and NED – E_0^* values for various LPBF studies processing SS316L powder

Number	Process Parameters					Relative Density (%)	NED (E_0^*)	Ref
	Laser power (W)	Scanning speed (mm/s)	Layer thickness (µm)	Hatch spacing (µm)	Spot size (µm)			
1	150	400	30	80	70	98.93	10.442	[38]
2	180	1600	30	70	75	96	3.580	[26]
3	380	700	50	110	180	99.8	6.596	[39]
4	200	800	30	120	64	99.7	4.641	[40]
5	100	700	20	70	50	> 99	6.820	[22]
6	150	700	20	50	50	> 99	14.321	[22]
7	380	2000	50	35	80	99.9	7.256	[39]
8	100	200	50	122	200	> 99.5	5.569	[41]
9	200	220	50	122	200	> 99.5	11.139	[41]
10	195	1100	20	120	100	99.9	4.936	[25]
11	195	800	20	60	100	99.9	13.575	[25]

Table 2 The chemical composition of SS316L powder

Chemical composition								
Element	Fe	Cr	Ni	Mo	C	Mn	Si	Others
Wt (%)	Balance	17.6	12.6	2.34	0.016	0.89	0.57	0.13

Table 3 Physical properties of SS316L

Physical Properties of SS316L	Values	Units
Melting Temperature (T_m)	1648	K
Density (ρ)	7999	kg/m^3
Specific Heat (C_p)	500	$J/kg\ K$
Thermal Conductivity	16.2	W/mK
Thermal Diffusivity	4.06×10^{-6}	m^2/s
Absorptivity at 450 nm [18]	78.4	%

series stainless steels by its elevated nickel content. Also, the quantity of molybdenum incorporated into the chemical composition of SS316L in comparison to the stainless steel 304 series enhances its corrosion resistance in salt environments [7]. Additional specifications about SS316L powder are given in Table 3. The physical properties of the powder are obtained from the supplier's data sheet on the material.

Figure 2(a) shows the powder morphology under Scanning Electron Microscopy (SEM) with 500× magnification. Figure 2(b) shows the powder's particle size distribution, measured with Malvern Mastersizer 3000. The mean values of the Dv(10), Dv(50), and Dv(90) parameters for the powder sample are found to be 17.9 µm, 28.5 µm, and 43.9 µm, respectively. These values are comparable to those reported in the supplier's datasheet.

2.2 System development and operational procedures

Figure 3 illustrates the schematics of DAM technology. DAM integrates independently addressable fiber-coupled 450 nm multiple blue diode lasers into a custom scanning head, which is described in Fig. 3 as a Multi Laser Head (MLH). The MLH incorporates collimating and focusing lenses, which direct and focus the beams to achieve localised melting during the fabrication process. The MLH is mounted into an x–y-z linear stage, which allows it to move over the substrate by the intended scanning strategy. The laser configuration used in this study, illustrated in Fig. 3, consists of six blue diode lasers operating at a wavelength of 450 nm. Figure 3 highlights the configuration of the laser array, which comprises lasers with a diameter of 70 µm and a central distance between adjacent lasers of 90 µm at focus distance which is 27 mm for our MLH. Additionally, the laser beam profile has been measured using a NanoScan2sPryo/9/5 optical profilometer and is presented alongside MLH in Fig. 3. While the spot diameter of each laser is 70 µm in the laser configuration (see Fig. 3), the height of each laser spot increases to 107 µm in the laser beam profile (see Fig. 3). This discrepancy may arise from beam reflection due to the MLH. In the absence of a back-reflection

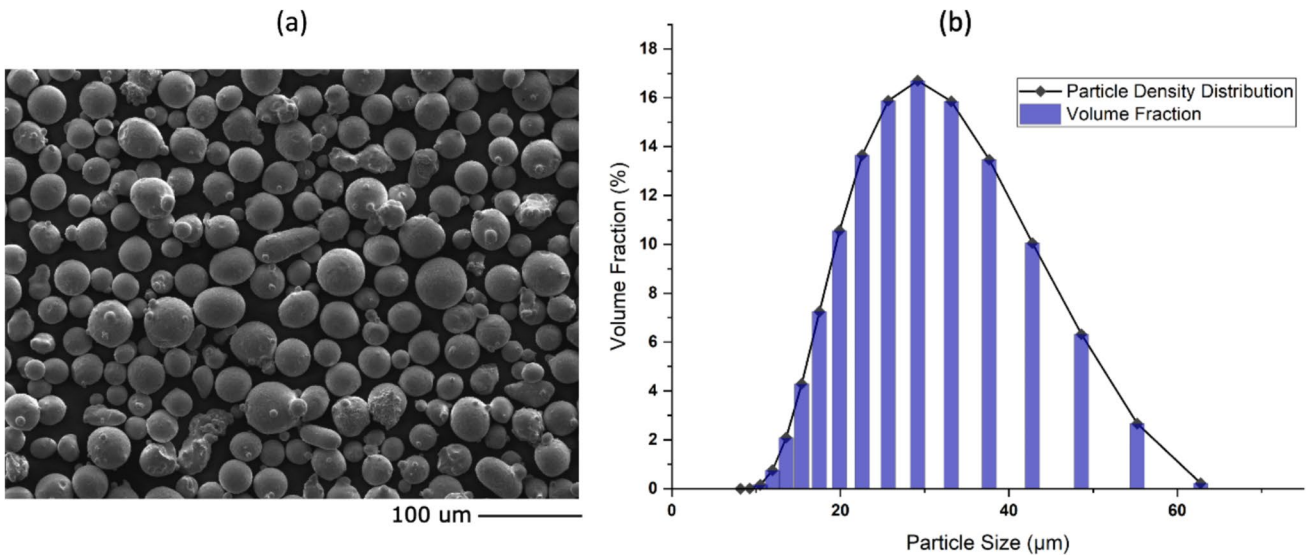

Fig. 2 **a** SEM image of SS316L powder, **b** particle size distribution of SS316L powder

element within the MLH assembly, the measurements could potentially be affected by the back reflection of the laser beams. Laser power loss due to the fiber connection between the diode lasers and the MLH is quantified using the Thorlabs PM400K5 power meter kit, and the output power of both lasers is maintained at ~ 3.5 W. Each laser in the configuration operates at an optical power output of 3.5 W, resulting in a total laser array power of 21 W, as detailed in Table 4. In addition to the MLH in the DAM system, there are two pistons corresponding to the reservoir and build platforms and powder delivery systems (see Fig. 3), which are similar to traditional LPBF machines. Argon gas is introduced into the custom-built chamber with oxygen content monitored with a sensor to maintain an oxygen level below 1000 ppm throughout the processing. An air knife is situated within the build chamber, this recirculates argon gas and prevents spatter falling onto the powder bed processing area. A 1 mm in thickness of powder is deposited over a metal substrate measuring 75×75 mm^2 and then laser processed. The use of a thick metal powder layer enables the quantification of melt-pool penetration depth.

2.3 Design of experiment

Single-layer experiments are conducted with the laser array configuration illustrated in Fig. 3. The scanning speeds and the hatch distance which is the central difference between lines of track parameters, as outlined in Table 4, are employed to fabricate thirty distinct single-layer samples, each measuring 6×4 mm^2. A stripe pattern is selected as the scanning strategy to produce single-layer samples. Table 4 illustrates the dimensions of the sample and the scanning strategy employed. The lasers are positioned perpendicular to the scanning direction (represented by the long stripes in Table 4) within the multi-laser spot configuration (see Fig. 3). The lasers remain active during processing, resulting in melt pool

Table 4 All process parameters and dimensions of the sample with scanning strategy in this work

Process parameters	Values	Units	
Laser Power	21 (6 x3.5)	W	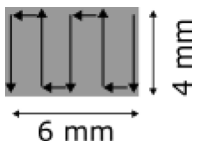
Hatch Distance	200,300,400	μm	
Scanning Speed	50-100-...-500	mm/min	

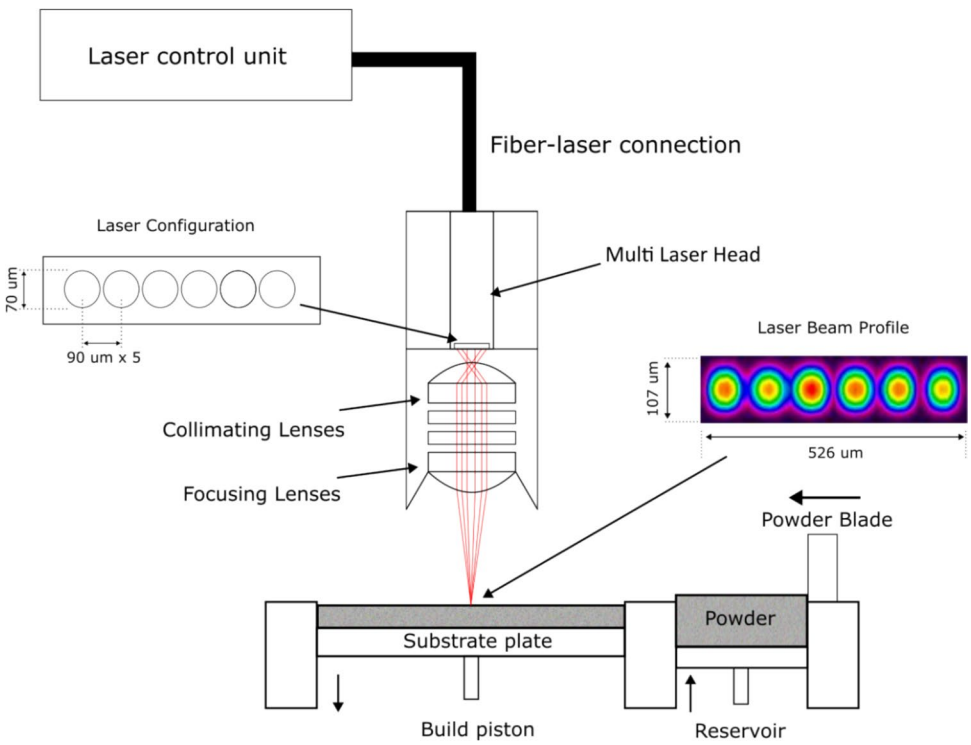

Fig. 3 The schematics of the DAM system with laser array configuration and its optical profile

overlaps that are parallel to the scanning direction (long stripes in Table 4), which is a consequence of the designated hatch distance parameter. In this study, the scanning strategy is designated as SS, and the hatch distance is denoted as HD.

2.4 Material characterisation

Each sample is mounted in a Bakelite to facilitate the automatic metallographic procedures. Initially, the samples are ground with waterproof grinding paper of progressively finer grits, ranging from P320 to P4000. The samples are cleaned using an ultrasonic cleaner, adding isopropanol. Subsequently, a 0.06 µm particle-sized colloidal silica is applied to achieve a mirror-like finish on the surface. Kalling's No.2 Reagent is used as an etching solution to distinguish the cellular structure of samples under sub-grain level.

Samples are examined using optical microscopy (OP) and scanning electron microscopy (SEM). The cross-sections of the single-layer samples have been examined under OP at 5 × and 10 × magnification. A microstructural investigation is conducted under SEM at 800 × and 5000 × magnification from the cross-sectional surfaces. The top surface of the single-layer samples is investigated using SEM at 35 × magnification to ascertain the quality of the surface in terms of balling and its morphology. Subsequently, the cross-sectional density of samples is quantified by utilising the Image J software [42], employing an optical thresholding technique. The relative densities of the samples are determined by measuring the optical microscopy images of each sample's cross-section, as illustrated in Fig. 4. Samples are cut and optical microscopy images are obtained from cross-sections to evaluate melt track characteristics in terms of melt track penetration into the powder bed. Relative density measurements are obtained from polished cross-sections by determining the region of interest, which encompasses the majority of samples (see dashed red rectangle in Fig. 4(h)).

The surface roughness is calculated by the Alicona Infinite Focus SL optically. The concept of surface roughness is a pervasive one in the literature, employed as a means of assessing the quality of a given part and of optimizing process parameters [21, 43, 44]. Vickers hardness measurements are performed on a cross-section of polished samples, with five individual measurements taken from each sample and averaged to eliminate extreme measurement points. Finally, X-ray diffraction (XRD) measurements are conducted using a PANalytical Aeris instrument over a range of 0° to 100° with a 10-min rotating scan.

3 Results

3.1 Melt pool characterisation of single-layer formation

One of the most important key process parameters in terms of single-layer formation is the hatch distance to eliminate poor connections between adjacent melt tracks. In addition, the hatch distance/melt pool overlap should not be set too high/low to produce fully melted structures without defects. Increasing the melt pool overlap increases the number of melt tracks on the manufactured part, which can have a negative effect on surface roughness [45]. Three different hatch distance values are used to understand melt track overlap to produce single-layer formation. 200 µm, 300 µm and 400 µm (HD200, HD300 and HD400) are the hatch distance parameters in this work (see Table 4). The melt track overlap between each laser track is calculated using Eq. 6. In this study, the beam profile width (b_w) is assumed to be equal to the melt track width. According to previous research on processing Ti6Al4V in DAM [4], no significant difference exists between the two. Another reason for this assumption is the lack of capability for in-situ measurements of the melt pool width during processing. Then, Eq. 7 is used to calculate the hatch distance according to the melt track overlap (m_o) in microns. HD200, HD300, and HD400 correspond to 60%, 40%, and 20% beam overlap respectively. Dong et al. highlighted the clear distinction between melt tracks, noting no overlap between them [46]. Furthermore, it was demonstrated that even 40% melt track overlap results in enhanced top surface morphology in terms of surface roughness. However, additional overlapping reduces the strength and plasticity of LPBF parts due to the formation of microcracks [46]. It has been demonstrated that a 25–50% overlap results in a stress release effect due to the re-scanning of previously scanned areas [47]. However, excessive overlap can prevent the preheating effect on a later track from the previous one. Consequently, it has been established that residual stresses increase with a high overlap ratio [47].

$$m_o[\mu m] = b_w[\mu m] * overlap\ percentage[\%] \tag{6}$$

$$HD[\mu m] = b_w[\mu m] - m_o[\mu m] \tag{7}$$

Figure 4 depicts optical micrographs of cross-sectional single-layer samples under 5 × magnification for SS50, SS100, SS150, SS200, SS450, and SS500. The depth of the melt track at the bottom right of each micrograph and the surface roughness at the bottom left of each micrograph for all hatch distance values (e.g. HD200, HD300, and HD400) are presented. The depth of the melt track is measured from

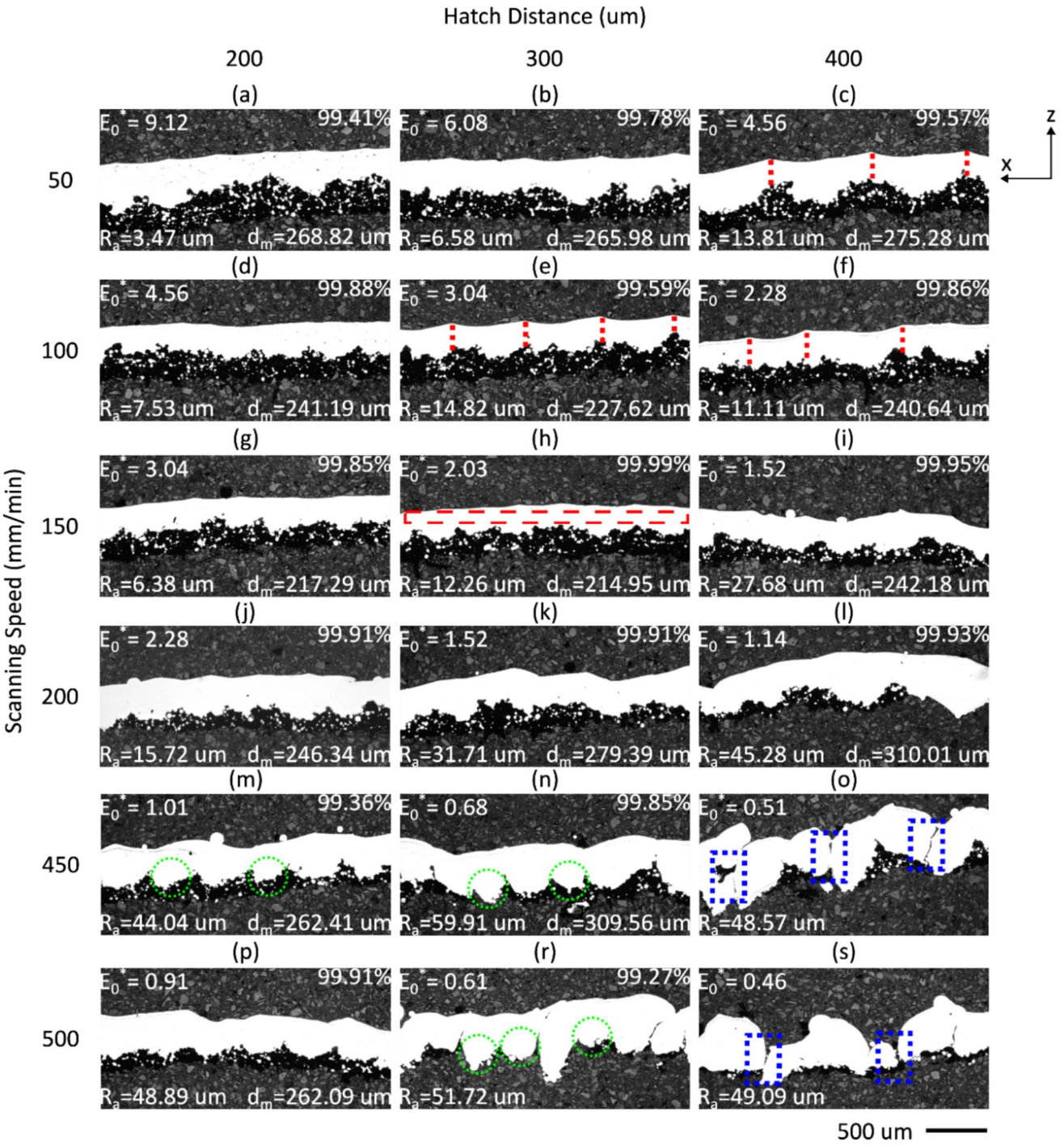

Fig. 4 Optical microscopy images of the cross-section of single-layer samples with SS50-SS200 by 50 increments and SS450 and SS500 for HD200, HD300, and HD400 including melt track depth (d_m) at the right bottom corner, surface roughness (Ra) at the bottom left corner, relative energy density at the right top corner, and normalised energy density at the left top corner of each micrograph

microscopy images, as illustrated in Fig. 4. Ten measurements are taken from each microscope, comprising both deep and shallow parts of the melt track geometry. The results are averaged and are presented in the bottom right corner of the micrographs in Fig. 4. Further micrographs, spanning the range from SS300 to SS400, are not included here due to space limitations. It is evident that an increase in hatch distance results in a transformation of the cross-section

of samples into a wave structure. This fluctuation is further emphasised by the addition of vertical red dotted lines in Figs. 4(c), (e), and (f). The relative density values and normalised energy density values are provided in the upper right and left corners of Figs. 4(a) to (s), respectively. It can be observed that the relative density values of both samples exceed 99%. Furthermore, the normalised energy density values exhibit a notable decline, ranging from 9.12 to 0.46, across the samples from SS50HD200 to SS500HD400 due to an increase in scanning speed and hatch distance.

The melt track depths (d_m) are examined individually for each hatch distance set. At SS50 (Figs. 4(a) to (c)) the melt track depth is greater compared to higher speeds such as SS100 and SS150 (see Figs. 4(d) to (f) and Figs. 4(g) to (i)) for each data set. For example, the melt depth for SS50HD200 is 268.82 µm while the melt track depths for SS100HD200 and SS150HD200 are 241.19 µm and 217.29 µm respectively. As the scanning speed is increased, the energy density values decrease (for details, please refer to the top left corner of Figs. 4(a) to 4(s)). Accordingly, the melt track depth trend exhibits a downward trajectory from SS50 to SS150. The reduction in the melt track depth is also attributed to scanning speed, as demonstrated by Alsaddah et al. [5]. Furthermore, the depth of the melt track observed in the samples increases following the SS150. This is attributed to the balling issue, which has been previously validated in other DAM studies conducted at the single-layer formation section of Ti6Al4V [6].

A significant trend is observed in the same hatch distance set, whereby an increase in scanning speed leads to a notable decline in surface flatness and an accompanying rise in surface roughness (see Figs. 4(a) to (c) and Figs. 4(g) to (i)) [48]. The increase in surface roughness observed at low speeds, such as SS50 to SS150, can be attributed to spattering, which will be demonstrated with SEM images in Sect. 3.3. The surface roughness is observed to increase due to poor bonding and discontinuity on samples at SS450 and SS500 for HD400, as illustrated by the dotted blue rectangle in Figs. 4(o) and (s). Additionally, the poor surface roughness observed at SS450 and SS500 for HD200 and HD300 can be attributed to balling problems, which are represented by green circles in Figs. 4(m), (n), and (r).

3.2 Relative density measurements

The method for measuring the relative density of the sample is described in Sect. 2.4. Only the relative density of samples that have a higher scanning speed than 300 mm/min at HD400 is not measured due to the discontinuous nature of the sample due to poor overlap [49] at higher scanning speeds [50] (see Figs. 4(o) and (s)).

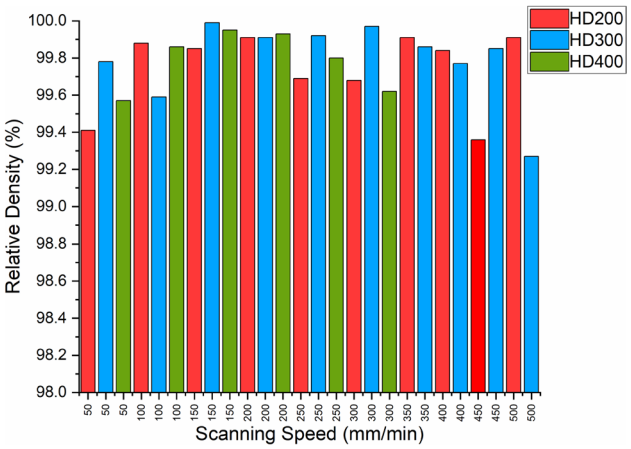

Fig. 5 The relative density values of samples from polished cross-sections

Figure 5 illustrates the relative densities of samples from SS50HD200 to SS500HD300, apart from SS350HD400, SS400HD400, SS450HD400, and SS500HD400. It can be observed that the relative density values of all samples exceed 99%. The utilisation of a laser configuration enables the successful melting and fusion of the feedstock, resulting in the absence of significant porosity between each track.

The density values for both the HD300 and HD400 samples are comparatively higher than those of samples with HD200, particularly at lower speeds, such as SS50, SS150, and SS250 (see Fig. 5). Figure 6 depicts the cross-sectional surfaces of select samples at × 10 magnification, accompanied by relative density values that facilitate a more detailed analysis of porosity in comparison to the data presented in Fig. 5. The relative density values are displayed in the bottom right corners of the micrographs presented in Fig. 6.

The presence of minor spherical pores is indicated by red circles in samples treated with HD200 (see Figs. 6(a), (d), (g), (j)). In contrast, the number of spherical pores observed in samples treated with HD300 is relatively low in comparison to the number of pores present in HD200 samples. These pores are represented by blue circles in Figs. 6(b), and (e)). Furthermore, a slight decrease in porosity is observed with an increase in scanning speed at samples with HD200 (see the first column of Fig. 6). The porosity of the samples containing HD200 is found to be greater at slower scanning speeds. Porosity in LPBF samples can be classified into three main categories: gas porosity, lack of fusion, and delamination between subsequent layers [51]. Pores that originated in samples with HD200 can be identified as gas porosity, given their spherical shape and the conditions under which they occurred

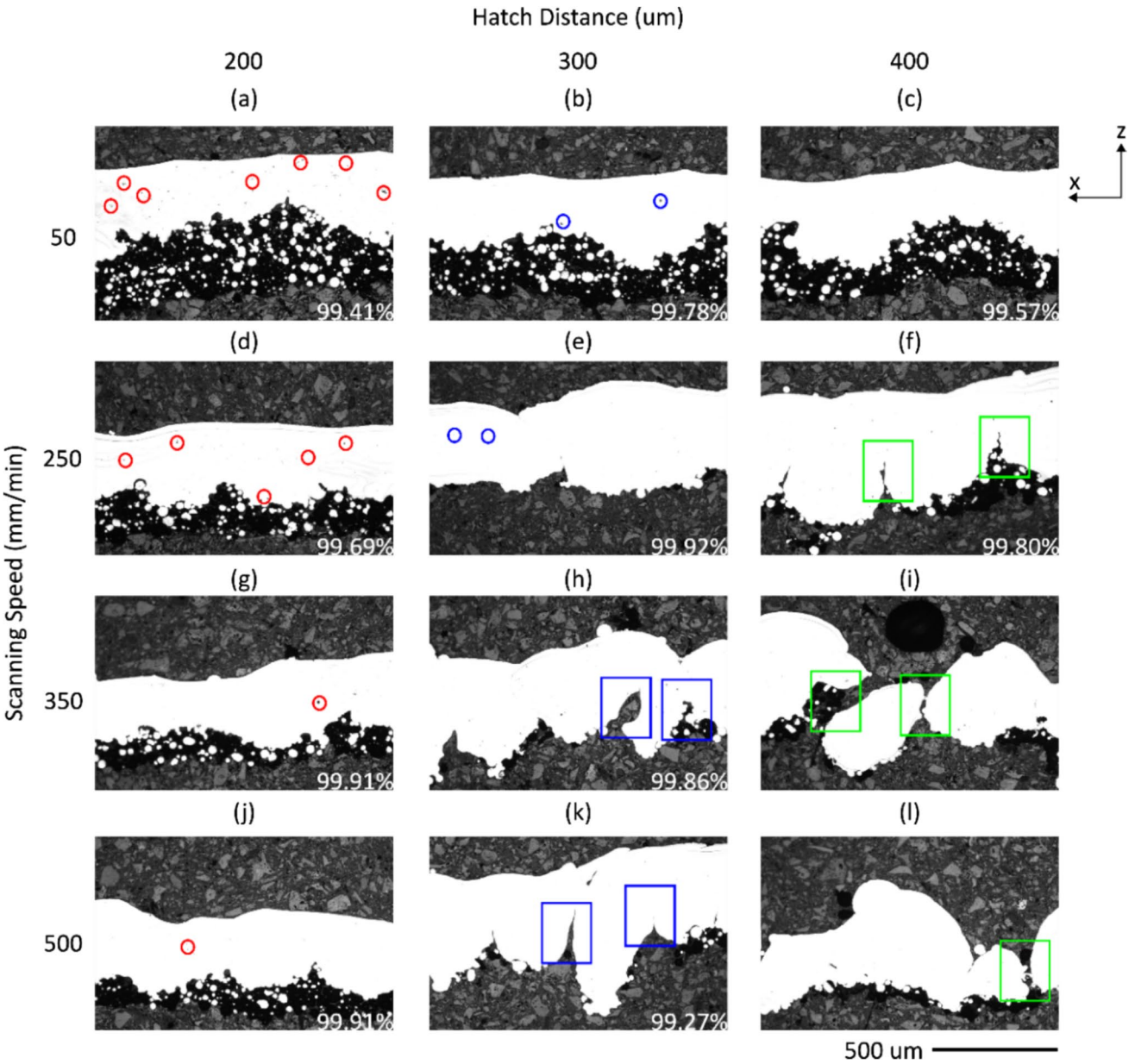

Fig. 6 Cross-sectional surface of samples with SS50, SS250, SS350, and SS500 at HD200, HD300, and HD400 with relative density values at the bottom left corner of each sample

(single-layer formation). An excessive degree of overlap in the melt track can result in a notable rise in temperature within the melt pool, which may subsequently give rise to several thermal issues [52]. It is hypothesized that the elevated temperature in the melt pool at slow scanning speeds results in vaporization. The spherical shape of the gas porosity is the result of the entrapped gas caused by the vapour pressure [53]. It is also stated that too low hatch distance at slow scanning leads to a decrease in relative density [54]. As the scanning speed is increased, the porosity of the samples with HD300 shows a slight increase (see the second column in Fig. 6) like the literature work in LPBF SS316L [55]. Additionally, some discontinuities are observed at the base of the sample (see the blue rectangles in Figs. 6(h) and (k)). An additional increase in hatch distance results in the formation of distinct cross-sectional divisions within the samples (as illustrated by the green rectangles in Figs. 6(f), (i), and (l)). The hypothesis that an increase in hatch distance will increase porosity has been previously validated [56].

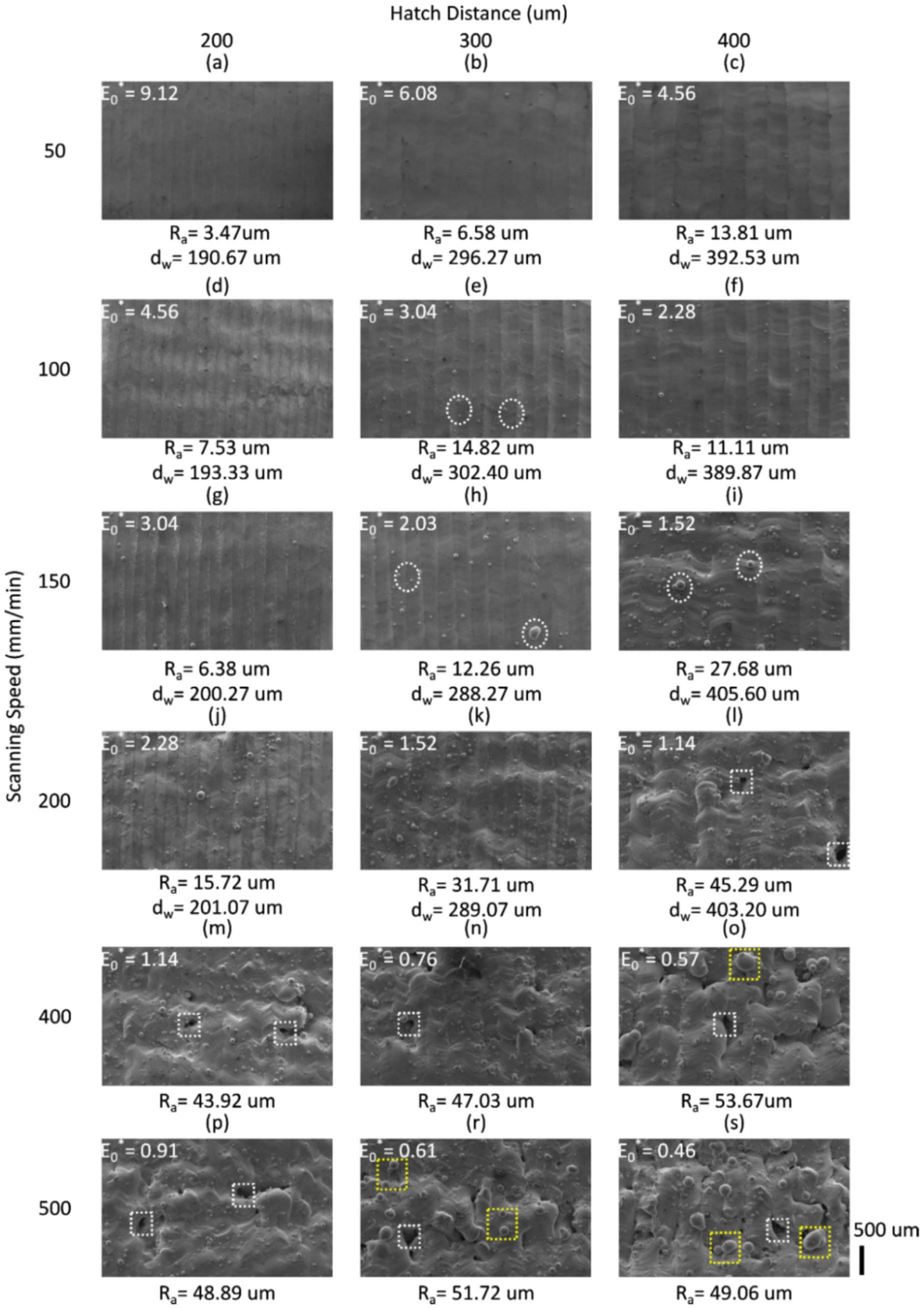

Fig. 7 SEM images of the top surfaces of single-layer samples with SS50-SS200 by 50 increments and SS400 and SS500 for HD200, HD300, and HD400 including melt track width and surface roughness at the below and normalised energy density (NED) values at the top left corner

3.3 Top surface quality in terms of SEM investigation

Figure 7 shows SEM micrographs of the top surfaces of single-layer samples at 35 × magnification for SS50, SS100, SS150, SS200, SS400, and SS500. Other micrographs are not shown here due to space considerations as in Fig. 4, but in Fig. 7 micrographs of SS400 are used in contrast to SS450 in Fig. 4 to show another range of sample morphology.

The NED values for each sample are shown in the top left-hand corner of each micrograph in Fig. 7, in addition to the surface roughness and melt track width (d_w) shown below each micrograph. The sample in Fig. 7(a) (SS50HD200 which has the highest NED value among all samples in this work) gives the lowest surface roughness result of all the samples with a Ra value of 3.47 µm. The surface quality deteriorates as the scanning speed increases for certain hatch distance values. Furthermore, the surface quality deteriorates as the hatch distance increases for the same set of scanning speeds [57]. The NED values range from 9.12 to 0.46 and are calculated using Eq. 4. Although the relationship between energy density values and surface roughness will be addressed subsequently, it can be observed that high NED values are indicative of superior surface quality in comparison to lower NED values (see Figs. 7(a) to (s)). In particular, when the energy input is below 1.52, there is a marked increase in surface roughness (see Figs. 7(l) and (m) or Figs. 7(n) to (o)) as a result of a lack of fusion [25]. The correlation between NED and surface roughness values primarily arises from variations in scanning speed.

The surface quality of the specimens deteriorates for low-speed specimens such as SS100HD300, SS150HD300, and S150HD400 thanks to multiple spatters on the top surface of the samples are shown in Figs. 7(e), (h), and (i). Spatter are represented by dotted white circles in Figs. 7(e), (h), and (i). After Fig. 7(l) to (s), the surface roughness increases due to poor top surface morphology, including balling problems. Figure 7(l) to (s) shows top surface porosity defects as dotted white rectangles. Melt traces become entangled when the scanning speed exceeds 200 mm/min, and this degrades the integrity of the samples. Balling is also observed on the top surfaces of samples at scanning speeds above 400 mm/min, shown as dotted yellow squares in Fig. 7(o), (r), and (s). The utilisation of high scanning speeds has been identified as a contributing factor to the formation of discontinuities and voids between tracks, which are commonly attributed to balling defects [58].

The melt track width of each sample is shown below each micrograph, except for further SS400HD200 samples, to allow the detection of melt track boundaries due to distortions in melt tracks, pores, balling, and lack of fusion problems. Melt track width increases as the hatch distance increases. For instance, the melt track width increases from 190.67 µm to 392.53 µm for HD200 and HD400 respectively, as shown in Figs. 6(a) to (c). In the same data set, there is no significant difference in melt track width as a function of scan speed. For example, the melt track width is 288.27 µm and 289.07 µm for samples SS150HD300 and SS200HD300 respectively.

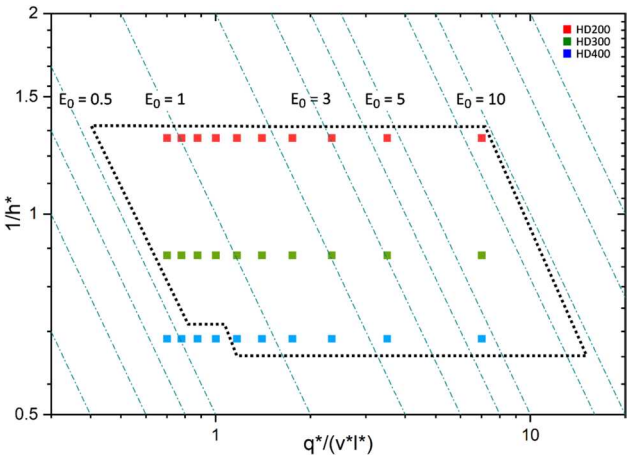

Fig. 8 The Normalised Energy Density (NED – E_0^*) mapping for all samples in this study is presented over base normalised energy density values, which are indicated by dashed lines. Samples that have > 99% relative density are confined with dotted polygon

3.4 Normalised energy density calculations

The NED values of all DAM samples, ranging from 0.46 to 9.12, are illustrated over constant NED contours, which are depicted as dotted lines in Fig. 8. The red rectangles represent samples treated with HD200, the green rectangles indicate samples treated with HD300, and the blue rectangles denote samples treated with HD400. The black dotted polygonal area in Fig. 8 represents samples with a relative density of greater than 99%. A total of four samples have been excluded from the region on the grounds of severe discontinuity in their cross-sectional structure. Accordingly, relative density measurements are not performed on these samples.

Table 5 shows surface roughness values and the normalised energy density (NED) values for all samples varying hatch distance and scanning speed with Eq. 4. As mentioned in the introduction, NED values for LPBF literature work related to SS316L range between 3 to 15. NED values of DAM samples in this work change from 9.12 to 0.46 and NED values of some samples equal each other due to

Table 5 Normalised energy density (NED) calculation for all process parameters set with relative density and surface roughness measurements

Process Parameters		Normalised Energy Density (E_0^*)	Relative Density (%)	Surface Roughness (μm)
SS (mm/min)	HD (μm)			
50	200	9.12	99.41	3.469
50	300	6.08	99.78	6.577
50	400	4.56	99.57	13.814
100	200		99.88	7.534
100	300	3.04	99.59	14.824
150	200		99.85	6.380
100	400	2.28	99.86	11.106
200	200		99.91	15.720
150	300	2.03	99.99	12.259
250	200	1.82	99.69	11.537
150	400	1.52	99.95	27.680
200	300		99.91	31.713
300	200		99.68	25.893
350	200	1.30	99.91	28.546
250	300	1.22	99.92	46.810
200	400	1.14	99.93	45.278
400	200		99.77	43.921
300	300	1.01	99.97	57.379
450	200		99.36	44.043
250	400	0.91	99.8	40.435
500	200		99.91	48.887
350	300	0.87	99.86	61.062
300	400	0.76	99.62	44.756
400	300		99.77	47.025
450	300	0.68	99.85	59.907
350	400	0.65	–	47.466
500	300	0.61	99.27	51.718
400	400	0.57	–	53.665
450	400	0.51	–	48.572
500	400	0.46	–	49.060

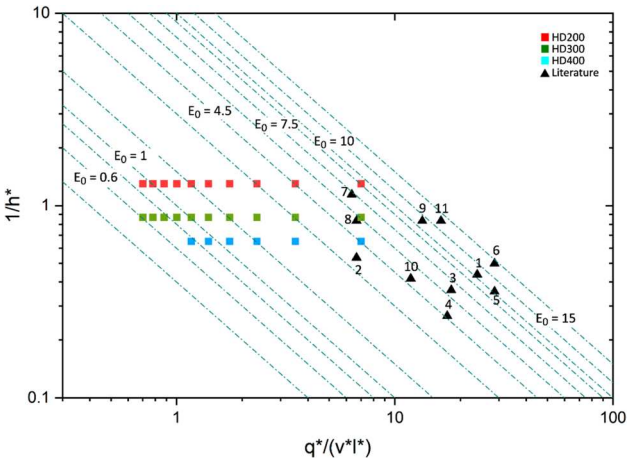

Fig. 9 The Normalised Energy Density (NED – E_0^*) mapping samples that have > 99% relative density in this study and literature LPBF studies (see Table 1 and Fig. 1) is presented over base normalised energy density values, which are indicated by dashed lines

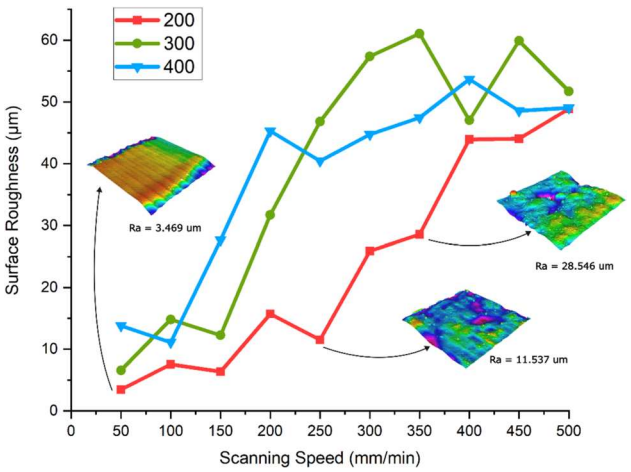

Fig. 10 Surface roughness (Ra) for all samples varying SS and HD values with exemplification of surface quality contour

the multiplication of hatch distance and scanning speed in Eq. 4. Additionally, Table 5 presents the relative densities for DAM samples. It is not feasible to determine the relative density of samples SS350HD400, SS400HD400, SS450HD400, and SS500HD400 (see Figs. 4(o) and (s) and Figs. 5 (i) and (l)) due to a substantial discontinuity along the crooked cross-section surface. The corresponding energy density values are 0.65, 0.57, 0.51, and 0.46, respectively (see Table 5).

Figure 9 facilitates the observation of both the existing literature on LPBF and the DAM samples (relative density of samples higher than 99%) presented in this paper by mapping them into the same graph which contains constant base NED values. Initially, literature works are obtained with varying hatch distance values to facilitate comprehension according to normalised energy but independent of the y-axis. Consequently, the values are mapped onto constant NED values to ensure consistency across the data set. Normalised energy density values for literature works typically range from 4.641 to 14.32 (see Table 1), enabling the fabrication of high-density (> 99%) samples. DAM facilitates the processing of fully melted and fused single-layer parts from 0.61 to 9.12 in terms of NED value, utilizing 450 nm blue diode lasers (the absorptivity of the SS316L powder increases by approximately 10% when a 450 nm diode laser is employed instead of a 1070 nm fiber laser [18]). It is also relevant to note that the DAM SS316L samples fabricated in this

study are of a single-layer structure. The energy requirement for multi-layer SS316L samples may be higher than that for single layers.

3.5 Surface roughness measurements

Figure 10 illustrates the surface roughness (Ra) values for all samples, which are obtained at varying scanning speeds (SS50 to SS500) and hatch distances (HD200, HD300, and HD400). The extent of melt pool overlap has a significant influence on the surface quality of the samples [57]. An increase in scanning speeds has been observed to result in a deterioration of surface quality, aside from the effect of hatch distance [48]. This is illustrated in Fig. 10, which presents several surface contours. It can be seen that Ra values for HD200 increase from 3.469 µm to 11.537 µm between SS50 and SS250. An additional increase in scanning speed results in an elevation of surface roughness to 28.546 µm when the scanning speed reaches 350 mm/min, as illustrated in Fig. 10. Increased scanning speeds result in the formation of discontinuities and non-uniformity in the melt tracks, which can be attributed to balling defects [48, 50]. The occurrence of balling problems and discontinuity problems is illustrated in Figs. 7(l) to (s). A similar phenomenon is observed in both hatch distances, with surface roughness increasing significantly from 6.577 µm to 51.718 µm and from 13.814 µm to 49.06 µm for HD300 and HD400, respectively, while SS50 to SS500 (see Table 5).

In addition to the effect of scanning speed, an increase in hatch distance (a reduction in the extent of melt pool overlap) results in the formation of waviness on the top surface of the sample, which can be attributed to the presence of poor overlapping. The surface roughness values at a constant speed, such as SS150, are 6.38 µm, 12.259 µm, and 27.68 µm for HD200, HD300, and HD400, respectively. At high scanning speeds, such as those observed after SS250, surface roughness increases significantly in both HD300 and HD400 due to the formation of balling and porosity, as illustrated in Figs. 7(n) to (s). An increase in the amount of overlap in the melt pool ensures the compactness of the top surfaces [49].

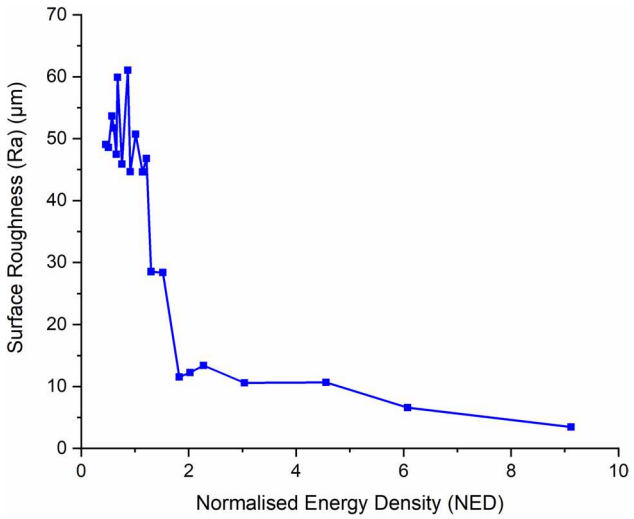

Fig. 11 The evolution of surface roughness (Ra) through each Normalised Energy Density (NED) value

Figure 11 depicts the surface roughness (Ra) values for varying energy density states. The normalised energy density values for certain specimens are identical, as evidenced by the comparison of SS100HD300 and SS150HD200, as illustrated in Table 5, where the energy density is observed to be 3.04. This phenomenon can be attributed to the multiplication of hatch distance and scanning speed. The surface roughness of samples with varying NED values is presented in Fig. 11. To illustrate, the energy density values for the SS300HD400 and SS400HD300 samples are identical at 0.76, while their respective roughness measurements are 44.756 µm and 47.025 µm. These values have been averaged and mapped in Fig. 11.

The optimal surface roughness (Ra) value is observed to be 3.469 µm, while the NED value is found to be 9.12. The process parameters are SS50 and HD200. Furthermore, the acceptable surface roughness results are 6.577 µm and 6.380 µm for the SS50HD300 and SS150HD200 samples, respectively, while the NED is 6.08 and 3.04, respectively, in terms of the existing literature on LPBF for SS316L [26, 45, 59]. The optimal surface roughness results are achieved within the range of 9.12 to 3.04 in terms of NED. A slight increase is observed below 3.04, which can be attributed to spattering, as illustrated in Figs. 7(e) and (h).

The surface roughness increases significantly when the NED value is below 1.30. The surface roughness of samples increases to 46.810 µm and 53.665 µm while NED equals 1.22 and 0.57 respectively (see Fig. 11 and Table 5). This is due to the presence of numerous small and large particles on the top surface, as illustrated in Figs. 7(i) to (s) with white dotted circles and yellow dotted rectangles. A further factor contributing to the decline in surface quality is the presence of porosity and discontinuity along the melt track, as illustrated in Figs. 7(l) to (s) by white dotted rectangles. A literature review reveals that as decrease in surface roughness and relative density is a primary cause of low energy density [38].

3.6 Phase determination

Figure 12(a) depicts the XRD profile of SS316L austenitic stainless-steel samples with varying scanning speeds (SS50, SS200, and SS500, which are selected to represent low, medium, and high scanning speeds) at HD200. Figure 12

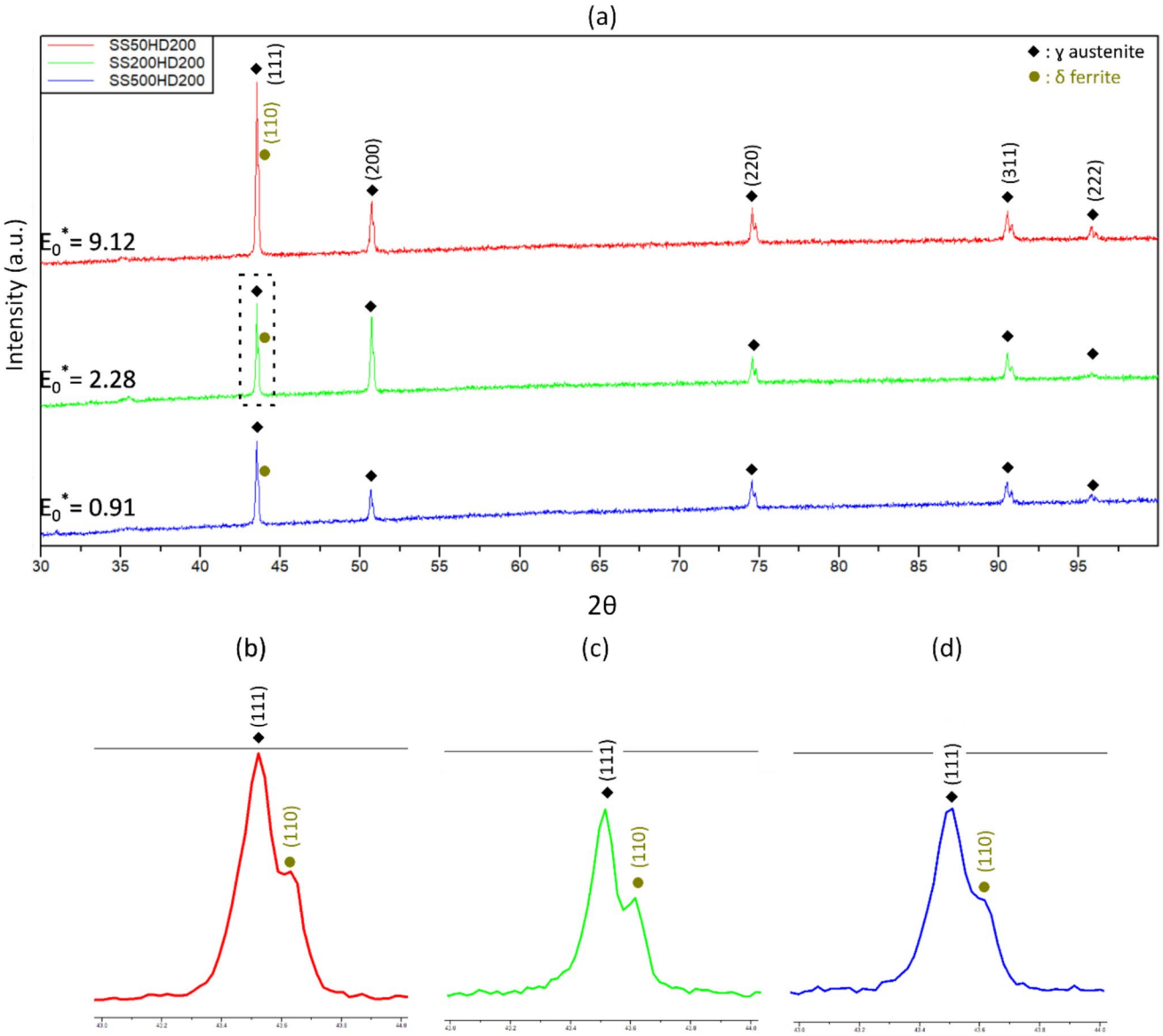

Fig. 12 **a** Phase analysis of SS50HD200, SS200HD200, and SS500HD200 samples with their NED values, **b**, **c**, and **d** represents the magnified versions of the dotted black rectangle for SS50HD200, SS200HD200, and SS500HD200 respectively

illustrates the existence of two distinct phases: face-centered cubic austenite (γ phase) and body-centered cubic ferrite (δ phase). The γ phase is corroborated by the presence of apparent diffraction peaks in the (111), (200), (220), (311), and (222) crystallographic planes, as observed in the LPBF SS316L sample referenced in the literature [60–63].

It is typically observed that samples produced through traditional LPBF processes exhibit only the γ austenite phase both in their as-built [60, 64–66] and heat-treated states [64–66]. In addition to LPBF, samples manufactured by alternative methods, including casting [67] and electron beam melting [68, 69], do not display the delta ferrite phase in their X-ray diffraction analysis. The presence of the small δ ferrite phase has also been documented in some of the literature on LPBF of SS316L, as referenced in [32, 39, 61, 62]. The ferrite phase is typically resistant to high temperatures, and the traditional LPBF process is unable to provide an adequate duration for the transformation into an austenitic phase [62]. Consequently, the observation of subsequent phases on samples may be prevented by the implementation of a high cooling rate at traditional LPBF [32]. It is anticipated by LPBF that the δ ferrite phase may serve to reinforce the γ austenite phase, which is susceptible to deformation [39, 62]. It has also been found that delta ferrite in austenitic steel welds increases the resistance to stress corrosion cracking caused by tensile stress in corrosive environments [70].

The second peak in Fig. 12(a), which corresponds to the (110) plane and follows the (111) crystallographic plane, serves to validate the existence of the δ ferrite phase in SS316L DAM samples. The peaks corresponding to the (111) and (110) crystallographic planes are represented in greater detail for the SS50HD200, SS200HD200, and SS500HD200 samples in the sequence (NED values of samples correspond to 9.12, 2.28, and 0.91 respectively), as illustrated in Figs. 12(b), (c), and (d), respectively. Furthermore, the regions explicitly depicted in Figs. 12(b), (c), and (d) are highlighted with a dotted black rectangle in Fig. 12(a) for the sole purpose of focusing attention on SS200HD200, due to the limited space available. The XRD analysis has validated that all samples (in terms of varying energy density, hatch distance, and scanning speed parameters) in this work exhibit delta ferrite phases. No coincident or specific parameters, like the previously mentioned LPBF literature works, have been identified that show a small amount of ferrite in the microstructure of DAM samples.

3.7 Microstructure analysis

The typical cellular dendritic microstructure of LPBF SS316L samples in sub-grain resolution has been previously documented in the literature [22, 25, 35, 71]. Liverani et al. have stated that the dimensions of each cell do not exceed 2 µm [22]. It has been demonstrated that an increase in energy density results in grain size coarsening in the microstructure of parts [71]. The determination of the overall grain size in LPBF SS316L samples is a challenging

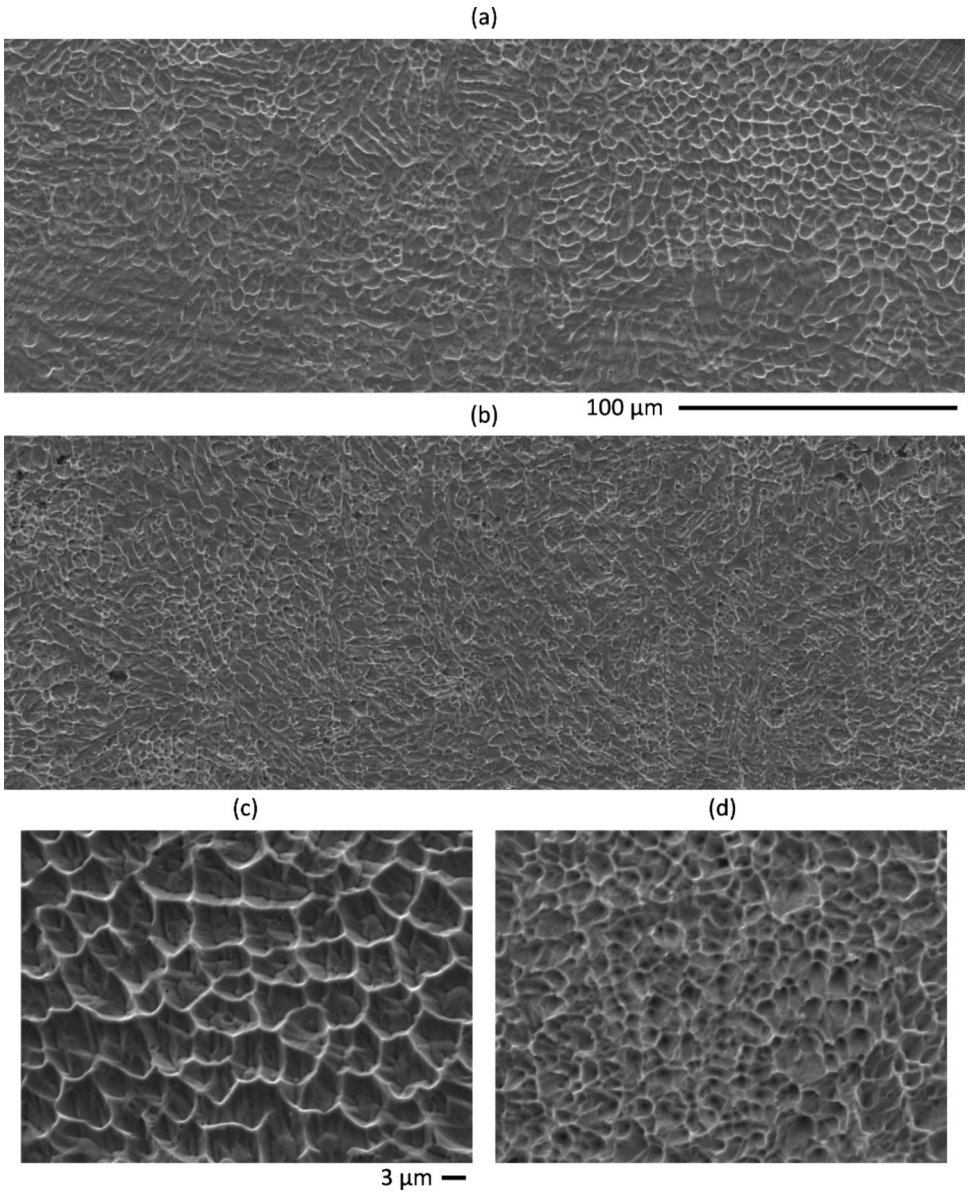

Fig. 13 SEM micrographs for sample **a** SS200HD400 under 800× magnification, **b** SS500HD400 under 800× magnification, **c** SS200HD400 under 5000× magnification (sample produced with 1.14 NED), **d** SS500HD400 under 800× magnification (sample produced with 0.46 NED)

process due to the significant degree of variation observed in the dimensions of the grains. In their study, Leicht et al. [25] examined both the grain size and the cell size within the grain for only one specific grain. It was revealed that the grain size increased from 200 µm in length and 10 µm in width to > 0.5 mm in length and 50 µm in width, while the energy density increased from 58 J/mm^3 to 203.1 J/mm^3. Additionally, the cell size was observed to increase from 361 ± 50 nm to 575 ± 50 nm at the same energy density increases were valid [25]. Larimian et al. [23] validated the relation between the scanning speed and grain size from cross-sectional surfaces both vertical and perpendicular to the building direction. It is acknowledged that a rise in scanning speed results in an augmentation of the cooling rate, and thus the cooling rate of the process is of paramount importance to the microstructure of the parts.

Figure 13 depicts the SEM micrograph images of the SS200HD400 and SS500HD400 samples at 800 × and 5000 × magnifications, respectively from cross-sectional surfaces. Figures 13(a) and (b) illustrate the broader section of the microstructure of the sample, wherein the cellular structure under the sub-grain level is discernible. Figures 13(c) and (d) illustrate the sub-grain level of the microstructure of the sample under 5000 × magnification. The size of the cellular structure exhibits fluctuations of 3–4 µm for SS200HD400 (see Fig. 13(c)), while a decrease of approximately 2 µm is observed for SS500HD400 (see Fig. 13(d)). The observed reduction in cell size can be attributed to a corresponding decrease in energy density values [25].

3.8 Hardness measurements

A review of the literature concerning the microhardness of LBPF SS316L components indicates that the Vickers hardness values of these components range from 160 to 240 HV. This is due to several factors, including the use of different scanning strategies, laser power, scanning speeds, and hatch distance [39, 45, 61, 72, 73]. However, most parts exhibit hardness values of approximately 225 HV. It was observed in the literature that the application of heat treatment on the as-built LPBF sample resulted in a negative impact on its microhardness. Sathies et al. [74] confirm that the sample that has undergone a heat treatment of two hours at 1100 °C and subsequent cooling in a furnace exhibits a microhardness of 175.6 HV, representing a 20% decrease compared to the as-built LPBF sample. Furthermore, microhardness values in samples produced via traditional methods, such as casting, are observed to be lower. Bartolomeu et al. [67] have indicated that the microhardness of as-cast and hot-pressed samples is 165 HV and 176 HV, respectively, while the hardness of the as-built LPBF sample is 229 HV.

The microhardness of DAM SS316L samples is relatively low in comparison to the values reported in the literature for LPBF, although some values are comparable to those reported for other samples, such as SS100HD300, SS200HD400, SS350HD400, and SS400HD400 (which are 206.66 HV, 196.2 HV, 197.6 HV, and 200.4 HV respectively). This discrepancy can be attributed to the reduced cooling rate in comparison to LPBF, a finding that has been corroborated in previous DAM studies [4, 5]. Furthermore, Song et al. [73], indicated that the sample utilizing a hexagonal scanning pattern exhibits reduced microhardness in comparison to alternative scanning strategies, with a value of approximately 180 HV. They ascribed the observed decline in hardness to a slower cooling rate [73]. The mean microhardness values for the sample in the same hatch distance set (see Fig. 14) indicate that the DAM samples exhibit greater hardness than the as-cast and heat-treated samples while displaying lower hardness than the as-built LPBF samples. The discrepancies between DAM and LPBF samples can also be attributed to the thickness disparity between the samples in addition to the cooling rate difference. In this study, DAM samples are produced in a single layer, whereas LPBF samples are manufactured in multiple layers.

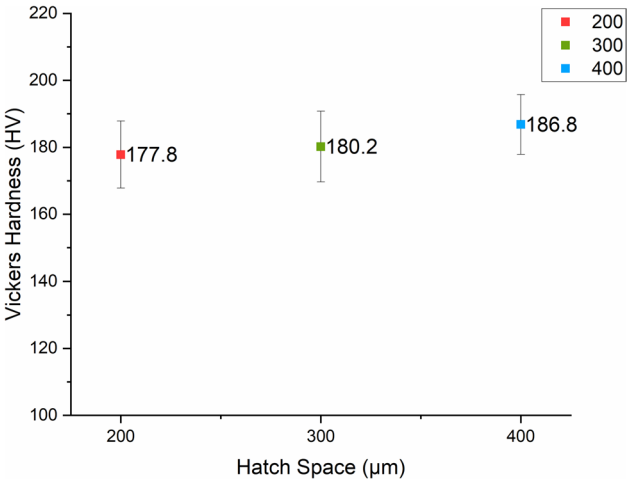

Fig. 14 The mean Vickers hardness values, with associated error bars for samples with varying scanning speeds for each hatch distance value from the cross-section

Lastly, all samples within the same hatch distance set are averaged, and the resulting values are represented by error bars in Fig. 14. It can be observed that the average microhardness values of samples increase when the hatch distance is increased. The mean microhardness value for HD200 is 177.8 HV, while that for HD400 is 186.8 HV. Additionally, the relative densities of samples within the same hatch distance set are averaged, except HD400, for which four samples with HD400 relative density could not be calculated due to discontinuity at cross-sectional surfaces. (see Fig. 4, Fig. 6 and Table 5). The relative density average of samples

with HD200 is found to be 99.74%, while that of samples with HD300 is 99.79%. A correlation exists between the averaged density and the averaged microhardness results. When the relative density of samples increases, the microhardness values of samples also increase [44].

4 Conclusion

This paper presents evidence of the small-scale manufacturing capability of DAM in SS316L, which is a highly desirable attribute in traditional LPBF processes due to its enhanced corrosion resistance and biocompatibility. SS316L represents a novel chapter in the field of DAM, exhibiting a higher density than its predecessor, Ti6Al4V feedstock. The DAM process enables the fabrication of fully melted and fused SS316L parts. It is observed that DAM enables a 99.99% dense part. It has been demonstrated that DAM represents a promising alternative to LPBF for the fabrication of samples with lower energy density requirements, due to the higher laser absorptivity of SS316L powder at a wavelength of 450 nm. The microstructural investigation reveals the significant presence of a δ ferrite phase, in addition to the main γ austenite phase in SS316L. This suggests that the presence of δ ferrite is evident in samples produced with varying energy inputs, without any coincidental procedures in previous LPBF works. It is hypothesized that a reduced cooling rate results in the formation of the δ ferrite phase. The presence of delta-ferrite in austenitic stainless-steel welds prevents cracking due to tensile stress in corrosive environments. The inherently slower cooling rate of DAM also results in an increase in the size of the cellular structure at the sub-grain level in comparison to LPBF work. While the cellular size in LPBF counterparts does not exceed 2 µm, the DAM samples display a cellular size of 3–4 µm. The present study compares the surface roughness and microhardness of DAM samples with those of LPBF samples from the literature. The sample with a slower scanning speed (SS50) and lower hatch distance (HD200) yielded superior results in terms of top surface defects and surface roughness measurements, with a value of 3.469 µm. Notable discrepancies in microhardness measurements between the DAM samples and previous LPBF works are attributed to the slower cooling rate. The hardness of the samples remains higher than that of the as-cast SS316L samples.

Author contribution Sefer Can Erman: Conceptualization, Methodology, Formal analysis, Investigation, Visualization, Writing—original draft. Alkim Aydin: Methodology, Visualization, Writing – review & editing. Kristian Groom: Conceptualization, Supervision. Kamran Mumtaz: Conceptualization, Project administration, Supervision, Writing – review & editing.

Funding This study was supported by the Turkish Government Ministry of Education and UK Research and Innovation, Engineering and Physical Sciences Research Council (EPSRC Grant EP/W024764/1).

Declarations

Conflict of interest The authors declare no conflict of interest.

References

1. Blakey-Milner B, Gradl P, Snedden G, Brooks M, Pitot J, Lopez E, Leary M, Berto F, du Plessis A (2021) Metal additive manufacturing in aerospace: a review. Mater Des 209. https://doi.org/10.1016/j.matdes.2021.110008
2. Haghdadi N, Laleh M, Moyle M, Primig S (2021) Additive manufacturing of steels: a review of achievements and challenges. J Mater Sci 56(1):64–107. https://doi.org/10.1007/s10853-020-05109-0
3. Zavala-Arredondo M, Boone N, Willmott J, Childs DTD, Ivanov P, Groom KM, Mumtaz K (2017) Laser diode area melting for high speed additive manufacturing of metallic components. Mater Des 117:305–315. https://doi.org/10.1016/j.matdes.2016.12.095
4. Alsaddah M, Khan A, Groom K, Mumtaz K (20220) Diode area melting of Ti6Al4V using 808 Nm laser sources and variable multi-beam profiles. Mater Des 215. https://doi.org/10.1016/j.matdes.2022.110518
5. Alsaddah M, Khan A, Groom K, Mumtaz K (2021) Use of 450–808 Nm diode lasers for efficient energy absorption during powder bed fusion of Ti6Al4V. Int J Adv Manuf Technol 113:2461–2480. https://doi.org/10.1007/s00170-021-06774-4/Published
6. Caglar H, Liang A, Groom K, Mumtaz K (2024) Multi-laser powder bed fusion of Ti6Al4V: diode area melting utilizing low-power 450 Nm diode lasers. J Mater Process Technol 325. https://doi.org/10.1016/j.jmatprotec.2024.118303
7. Sedriks AJ (1982) Corrosion resistance of austenitic Fe-Cr-Ni-Mo alloys in marine environments. Int Met Rev 27(1):321–353. https://doi.org/10.1179/imr.1982.27.1.321
8. Kong D, Ni X, Dong C, Lei X, Zhang L, Man C, Yao J, Cheng X, Li X (2018) Bio-functional and anti-corrosive 3D printing 316L stainless steel fabricated by selective laser melting. Mater Des 152:88–101. https://doi.org/10.1016/j.matdes.2018.04.058
9. Groarke R, Danilenkoff C, Karam S, McCarthy E, Michel B, Mussatto A, Sloane J, Neill AO, Raghavendra R, Brabazon D (2020) 316l stainless steel powders for additive manufacturing: relationships of powder rheology, size. Size Distribution to Part Properties. Materials 13(23):1–19. https://doi.org/10.3390/ma13235537
10. Muthukumaran V, Selladurai V, Nandhakumar S, Senthilkumar M (2010) Experimental investigation on corrosion and hardness of

ion implanted AISI 316L stainless steel. Mater Des 31(6):2813–2817. https://doi.org/10.1016/j.matdes.2010.01.007
11. Hryniewicz T, Rokosz K, Filippi M (2009) Biomaterial studies on AISI 316L stainless steel after magnetoelectropolishing. Materials 2(1):129–145. https://doi.org/10.3390/ma2010129
12. Čapek J, Machová M, Fousová M, Kubásek J, Vojtěch D, Fojt J, Jablonská E, Lipov J, Ruml T (2016) Highly porous, low elastic modulus 316L stainless steel scaffold prepared by selective laser melting. Mater Sci Eng C 69:631–639. https://doi.org/10.1016/j.msec.2016.07.027
13. Muthu SM, Mohana Bharathi C, Vishal Gukhan N, Vignesh Kumar S, Venkatesh Kannan M, Arivarasu M, Manikandan M, Arivazhagan N (2018) Hot corrosion studies on dissimilar weldments C-22 and AISI 316L in the molten salt K2SO4 + 60%wt NaCl Environment. Mater Today Proc 5(5):13340–13346. https://doi.org/10.1016/j.matpr.2018.02.326
14. Sánchez-Tovar R, Montañés MT, García-Antón J (2013) Effects of microplasma Arc AISI 316L welds on the corrosion behaviour of pipelines in LiBr cooling systems. Corros Sci 73:365–374. https://doi.org/10.1016/j.corsci.2013.04.025
15. Velázquez De La Hoz JL, Cheng K (2024) Investigation on the modeling and simulation of hydrodynamics in asymmetric conduction laser micro-welding of austenitic stainless steel and its process optimization. Proc Inst Mech Eng Part B J Eng Manuf 09544054241235839. https://doi.org/10.1177/09544054241235839
16. D'Andrea D (2023) Additive manufacturing of AISI 316L stainless steel: a review. Metals 13(8):1370. https://doi.org/10.3390/met13081370
17. Miyamoto I, Knorovsky GA (2008) Laser microwelding. Microjoining and nanojoining. Elsevier, pp 345–417. https://doi.org/10.1533/9781845694043.2.345
18. Brandau B, Da Silva A, Wilsnack C, Brueckner F, Kaplan AFH (2022) Absorbance study of powder conditions for laser additive manufacturing. Mater Des 216. https://doi.org/10.1016/j.matdes.2022.110591
19. Vilaro T, Colin C, Bartout JD (2011) As-fabricated and heat-treated microstructures of the Ti-6Al-4V alloy processed by selective laser melting. Metall Mater Trans Phys Metall Mater Sci 42(10):3190–3199. https://doi.org/10.1007/s11661-011-0731-y
20. Vrancken B, Thijs L, Kruth JP, Van Humbeeck J (2012) Heat treatment of Ti6Al4V produced by selective laser melting: microstructure and mechanical properties. J Alloys Compd 541:177–185. https://doi.org/10.1016/j.jallcom.2012.07.022
21. Song B, Dong S, Zhang B, Liao H, Coddet C (2012) Effects of processing parameters on microstructure and mechanical property of selective laser melted Ti6Al4V. Mater Des 35:120–125. https://doi.org/10.1016/j.matdes.2011.09.051
22. Liverani E, Toschi S, Ceschini L, Fortunato A (2017) Effect of Selective Laser melting (slm) process parameters on microstructure and mechanical properties of 316L austenitic stainless steel. J Mater Process Technol 249:255–263. https://doi.org/10.1016/j.jmatprotec.2017.05.042
23. Larimian T, Kannan M, Grzesiak D, AlMangour B, Borkar T (2020) Effect of energy density and scanning strategy on densification, microstructure and mechanical properties of 316L stainless steel processed via selective laser melting. Mater Sci Eng A 770:138455. https://doi.org/10.1016/j.msea.2019.138455
24. Tran HC, Lo YL (2019) Systematic approach for determining optimal processing parameters to produce parts with high density in selective laser melting process. Int J Adv Manuf Technol 105(10):4443–4460. https://doi.org/10.1007/s00170-019-04517-0
25. Leicht A, Rashidi M, Klement U, Hryha E (2020) effect of process parameters on the microstructure, tensile strength and productivity of 316L parts produced by laser powder bed fusion. Mater Charact 159. https://doi.org/10.1016/j.matchar.2019.110016
26. Alsalla HH, Smith C, Hao L (2018) Effect of build orientation on the surface quality, microstructure and mechanical properties of selective laser melting 316L stainless steel. Rapid Prototyp J 24(1):9–17. https://doi.org/10.1108/RPJ-04-2016-0068
27. Yang X-H, Jiang C-M, Ho J-R, Tung P-C, Lin C-K (2021) Effects of laser spot size on the mechanical properties of AISI 420 stainless steel fabricated by selective laser melting. Materials 14(16):4593. https://doi.org/10.3390/ma14164593
28. Gu D, Hagedorn YC, Meiners W, Meng G, Batista RJS, Wissenbach K, Poprawe R (2012) Densification behavior, microstructure evolution, and wear performance of selective laser melting processed commercially pure titanium. Acta Mater 60(9):3849–3860. https://doi.org/10.1016/j.actamat.2012.04.006
29. Hooper PA (2018) Melt pool temperature and cooling rates in laser powder bed fusion. Addit Manuf 22:548–559. https://doi.org/10.1016/j.addma.2018.05.032
30. Vysotskiy I, Malopheyev S, Zuiko I, Mironov S, Kaibyshev R (2022) Microstructure distribution in 17–4 PH martensitic steel produced by selective laser melting. Metall Mater Trans Phys Metall Mater Sci 53(12):4143–4147. https://doi.org/10.1007/s11661-022-06829-5
31. Thijs L, Verhaeghe F, Craeghs T, Humbeeck JV, Kruth J-P (2010) A study of the microstructural evolution during selective laser melting of Ti–6Al–4V. Acta Mater 58(9):3303–3312. https://doi.org/10.1016/j.actamat.2010.02.004
32. Tucho WM, Lysne VH, Austbø H, Sjolyst-Kverneland A, Hansen V (2018) Investigation of effects of process parameters on microstructure and hardness of SLM manufactured SS316L. J Alloys Compd 740:910–925. https://doi.org/10.1016/j.jallcom.2018.01.098
33. Farshidianfar MH, Khajepour A, Gerlich AP (2016) Effect of real-time cooling rate on microstructure in laser additive manufacturing. J Mater Process Technol 231:468–478. https://doi.org/10.1016/j.jmatprotec.2016.01.017
34. Gor M, Soni H, Singh Rajput G, Sahlot P (2022) Experimental investigation of mechanical properties for wrought and selective laser melting additively manufactured SS316L and MS300. Mater Today Proc 62:7215–7219. https://doi.org/10.1016/j.matpr.2022.03.511
35. Ahmed N, Barsoum I, Haidemenopoulos G, Al-Rub RKA (2022) Process parameter selection and optimization of laser powder bed fusion for 316L stainless steel: a review. J Manuf Process 75:415–434. https://doi.org/10.1016/j.jmapro.2021.12.064
36. Do DK, Li P (2016) The effect of laser energy input on the microstructure, physical and mechanical properties of Ti-6Al-4V alloys by selective laser melting. Virtual Phys Prototyp 11(1):41–47. https://doi.org/10.1080/17452759.2016.1142215
37. Thomas M, Baxter GJ, Todd I (2016) Normalised model-based processing diagrams for additive layer manufacture of engineering alloys. Acta Mater 108:26–35. https://doi.org/10.1016/j.actamat.2016.02.025
38. Wang D, Liu Y, Yang Y, Xiao D (2016) Theoretical and experimental study on surface roughness of 316L stainless steel metal parts obtained through selective laser melting. Rapid Prototyp J 22(4):706–716. https://doi.org/10.1108/RPJ-06-2015-0078

39. Sun Z, Tan X, Tor SB, Yeong WY (2016) Selective laser melting of stainless steel 316L with low porosity and high build rates. Mater Des 104:197–204. https://doi.org/10.1016/j.matdes.2016.05.035
40. Yan J, Zhou Y, Gu R, Zhang X, Quach WM, Yan M (2019) A comprehensive study of steel powders (316L, H13, P20 and 18Ni300) for their selective laser melting additive manufacturing. Metals 9(1). https://doi.org/10.3390/met9010086
41. Kurzynowski T, Gruber K, Stopyra W, Kuźnicka B, Chlebus E (2018) Correlation between process parameters, microstructure and properties of 316 L stainless steel processed by selective laser melting. Mater Sci Eng A 718:64–73. https://doi.org/10.1016/j.msea.2018.01.103
42. Schneider CA, Rasband WS, Eliceiri KW (2012) NIH image to ImageJ: 25 years of image analysis. Nat Methods 9(7):671–675. https://doi.org/10.1038/nmeth.2089
43. Ali U, Esmaeilizadeh R, Ahmed F, Sarker D, Muhammad W, Keshavarzkermani A, Mahmoodkhani Y, Marzbanrad E, Toyserkani E (2019) Identification and characterization of spatter particles and their effect on surface roughness, density and mechanical response of 17–4 PH stainless steel laser powder-bed fusion parts. Mater Sci Eng A 756:98–107. https://doi.org/10.1016/j.msea.2019.04.026
44. Greco S, Gutzeit K, Hotz H, Kirsch B, Aurich JC (2020) Selective laser melting (SLM) of AISI 316L—impact of laser power, layer thickness, and hatch spacing on roughness, density, and microhardness at constant input energy density. Int J Adv Manuf Technol 108(5–6):1551–1562. https://doi.org/10.1007/s00170-020-05510-8
45. Cherry JA, Davies HM, Mehmood S, Lavery NP, Brown SGR, Sienz J (2015) Investigation into the effect of process parameters on microstructural and physical properties of 316L stainless steel parts by selective laser melting. Int J Adv Manuf Technol 76(5–8):869–879. https://doi.org/10.1007/s00170-014-6297-2
46. Dong A, Du D, Toursangsaraki M, She H, Lei L, Sun B (2023) Overlap ratio and scanning strategy effects on laser powder bed fusion Ti6Al4V: numerical thermal modeling and experiments. Int J Adv Manuf Technol 125(7–8):3053–3067. https://doi.org/10.1007/s00170-023-10900-9
47. Chen C, Yin J, Zhu H, Xiao Z, Zhang L, Zeng X (2019) Effect of overlap rate and pattern on residual stress in selective laser melting. Int J Mach Tools Manuf 145:103433. https://doi.org/10.1016/j.ijmachtools.2019.103433
48. Yang KT, Kim MK, Kim D, Suhr J (2021) Investigation of laser powder bed fusion manufacturing and post-processing for surface quality of as-built 17–4PH stainless steel. Surf Coat Technol 422. https://doi.org/10.1016/j.surfcoat.2021.127492
49. Wang D, Yang Y, Su X, Chen Y (2012) Study on energy input and its influences on single-track, multi-track, and multi-layer in SLM. Int J Adv Manuf Technol 58(9–12):1189–1199. https://doi.org/10.1007/s00170-011-3443-y
50. Yuan W, Chen H, Cheng T, Wei Q (2020) Effects of laser scanning speeds on different states of the molten pool during selective laser melting: simulation and experiment. Mater Des 189. https://doi.org/10.1016/j.matdes.2020.108542
51. Kudzal A, McWilliams B, Hofmeister C, Kellogg F, Yu J, Taggart-Scarff J, Liang J (2017) Effect of scan pattern on the microstructure and mechanical properties of powder bed fusion additive manufactured 17–4 stainless steel. Mater Des 133:205–215. https://doi.org/10.1016/j.matdes.2017.07.047
52. Yadroitsev I, Yadroitsava I, Plessis AD, MacDonald E (2021) Fundamentals of laser powder bed fusion of metals. Elsevier. https://doi.org/10.1016/B978-0-12-824090-8.09001-6
53. Zai L, Zhang C, Wang Y, Guo W, Wellmann D, Tong X, Tian Y (2020) Laser powder bed fusion of precipitation-hardened martensitic stainless steels: a review. Metals 10(2):255. https://doi.org/10.3390/met10020255
54. Chen Z, Wei Z, Wei P, Chen S, Lu B, Du J, Li J, Zhang S (2017) Experimental research on selective laser melting AlSi10Mg alloys: process, densification and performance. J Mater Eng Perform 26(12):5897–5905. https://doi.org/10.1007/s11665-017-3044-5
55. Li R, Liu J, Shi Y, Du M, Xie Z (2010) 316L stainless steel with gradient porosity fabricated by selective laser melting. J Mater Eng Perform 19(5):666–671. https://doi.org/10.1007/s11665-009-9535-2
56. Kluczyński J, Śnieżek L, Grzelak K, Mierzyński J (2018) The influence of exposure energy density on porosity and microhardness of the SLM additive manufactured elements. Materials 11(11):2304. https://doi.org/10.3390/ma11112304
57. Dong Z, Liu Y, Wen W, Ge J, Liang J (2018) Effect of hatch spacing on melt pool and as-built quality during selective laser melting of stainless steel: modeling and experimental approaches. Materials 12(1):50. https://doi.org/10.3390/ma12010050
58. Li R, Liu J, Shi Y, Wang L, Jiang W (2012) Balling behavior of stainless steel and nickel powder during selective laser melting process. Int J Adv Manuf Technol 59(9–12):1025–1035. https://doi.org/10.1007/s00170-011-3566-1
59. Aqilah DN, Mohd Sayuti AK, Farazila Y, Suleiman DY, Nor Amirah MA, Wan Nur Izzati WB (2018) Effects of process parameters on the surface roughness of stainless steel 316L parts produced by selective laser melting. J Test Eval 46(4):1673–1683. https://doi.org/10.1520/JTE20170140
60. Choi J-P, Shin G-H, Brochu M, Kim Y-J, Yang S-S, Kim K-T, Yang D-Y, Lee C-W, Yu J-H (2016) Densification behavior of 316L stainless steel parts fabricated by selective laser melting by variation in laser energy density. Mater Trans 57(11):1952–1959. https://doi.org/10.2320/matertrans.M2016284
61. Shin W-S, Son B, Song W, Sohn H, Jang H, Kim Y-J, Park C (2021) Heat treatment effect on the microstructure, mechanical properties, and wear behaviors of stainless steel 316L prepared via selective laser melting. Mater Sci Eng A 806:140805. https://doi.org/10.1016/j.msea.2021.140805
62. Jeyaprakash N, Saravana Kumar M, Yang C-H, Cheng Y, Radhika N, Sivasankaran S (2024) Effect of microstructural evolution during melt pool formation on nano-mechanical properties in LPBF based SS316L parts. J Alloys Compd 972:172745. https://doi.org/10.1016/j.jallcom.2023.172745
63. Filimonov AM, Rogozin OA, Firsov DG, Kuzminova YO, Sergeev SN, Zhilyaev AP, Lerner MI, Toropkov NE, Simonov AP, Binkov II, Okulov IV, Akhatov IS, Evlashin SA (2020) Hardening of additive manufactured 316L stainless steel by using bimodal powder containing nanoscale fraction. Materials 14(1):115. https://doi.org/10.3390/ma14010115
64. Salman OO, Gammer C, Chaubey AK, Eckert J, Scudino S (2019) Effect of heat treatment on microstructure and mechanical properties of 316L steel synthesized by selective laser melting. Mater Sci Eng A 748:205–212. https://doi.org/10.1016/j.msea.2019.01.110
65. Waqar S, Liu J, Sun Q, Guo K, Sun J (2020) Effect of post-heat treatment cooling on microstructure and mechanical properties of selective laser melting manufactured austenitic 316L stainless steel. Rapid Prototyp J 26(10):1739–1749. https://doi.org/10.1108/RPJ-12-2019-0320
66. Zhou C, Wang J, Hu S, Tao H, Fang B, Li L, Zheng J, Zhang L (2020) Enhanced corrosion resistance of additively manufactured 316L stainless steel after heat treatment. J Electrochem Soc 167(14):141504. https://doi.org/10.1149/1945-7111/abc10e
67. Bartolomeu F, Buciumeanu M, Pinto E, Alves N, Carvalho O, Silva FS, Miranda G (2017) 316L stainless steel mechanical and

tribological behavior—a comparison between selective laser melting, hot pressing and conventional casting. Addit Manuf 16:81–89. https://doi.org/10.1016/j.addma.2017.05.007
68. Wang C, Tan X, Liu E, Tor SB (2018) Process parameter optimization and mechanical properties for additively manufactured stainless steel 316L parts by selective electron beam melting. Mater Des 147:157–166. https://doi.org/10.1016/j.matdes.2018.03.035
69. Zhong Y, Rännar L-E, Liu L, Koptyug A, Wikman S, Olsen J, Cui D, Shen Z (2017) Additive manufacturing of 316L stainless steel by electron beam melting for nuclear fusion applications. J Nucl Mater 486:234–245. https://doi.org/10.1016/j.jnucmat.2016.12.042
70. Kain V (2011) Stress Corrosion Cracking (SCC) in stainless steels. Stress Corrosion Cracking, Elsevier, pp 199–244. https://doi.org/10.1533/9780857093769.3.199
71. Wang D, Song C, Yang Y, Bai Y (2016) Investigation of crystal growth mechanism during selective laser melting and mechanical property characterization of 316L stainless steel parts. Mater Des 100:291–299. https://doi.org/10.1016/j.matdes.2016.03.111
72. Yusuf SM, Chen Y, Boardman R, Yang S, Gao N (2017) Investigation on porosity and microhardness of 316L stainless steel fabricated by selective laser melting. Metals 7(2). https://doi.org/10.3390/met7020064
73. Song Y, Sun Q, Guo K, Wang X, Liu J, Sun J (2020) Effect of scanning strategies on the microstructure and mechanical behavior of 316L stainless steel fabricated by selective laser melting. Mater Sci Eng A 793. https://doi.org/10.1016/j.msea.2020.139879
74. Sathies T, Kumaran M, Bharathiraja G, Balaji NS, Unnikrishnan TG, Senthil Kumar V (2022) Investigations on the effect of heat treatment on laser powder bed fusion built SS316L alloy. Mater Today Proc 62:5411–5414. https://doi.org/10.1016/j.matpr.2022.03.699